THE JOURNAL OF PHYSICAL CHEMISTRY C

Article

Cite This: J. Phys. Chem. C 2019, 123, 8133−8144

pubs.acs.org/JPCC

Hybrid-DFT Modeling of Lattice and Surface Vacancies in MnO

Andrew J. Logsdail,*[,†] Christopher A. Downing,[‡,¶] Thomas W. Keal,[¶] Paul Sherwood,[¶] Alexey A. Sokol,[‡] and C. Richard A. Catlow[‡,†,§]

[†]Cardiff Catalysis Institute, School of Chemistry, Cardiff University, Cardiff, CF10 3AT, United Kingdom

[‡]Kathleen Lonsdale Materials Chemistry, Department of Chemistry, University College London, 20 Gordon Street, London, WC1H 0AJ, United Kingdom

[¶]Scientific Computing Department, STFC Daresbury Laboratory, Daresbury, Warrington, WA4 4AD, United Kingdom

[§]UK Catalysis Hub, Research Complex at Harwell, Science and Technology Facilities Council Rutherford Appleton Laboratory, Harwell Science and Innovation Campus, Oxon, OX11 0QX, United Kingdom

Supporting Information

ABSTRACT: We have investigated the properties of defects in MnO bulk and at (100) surfaces, as used in catalytic applications, using hybrid-level density functional theory (i.e., inclusion of exact exchange within the exchange-correlation evaluation) in a hybrid QM/MM embedded-cluster approach. Initially, we calculate the formation energy for bulk Mn and O vacancies, comparing charged-defect compensation with charge carriers at the Fermi Level (ϵ_f) and through Schottky defect formation. Oxygen vacancies were also investigated at the (100) surface, where the vacancy formation energy is very similar to the bulk. Defect levels associated with the most stable vacancies are calculated using the ΔSCF method: all are positioned mid band gap, with surface environments failing to alter strongly the overall nature of the defect relative to bulk. Chemical activity of the (100) MnO surface was considered through the adsorption of a probe CO_2 molecule, which is considered the initial step in the transformation of CO_2 into hydrocarbons. CO_2 adsorption was strongest over a neutral oxygen vacancy, where the associated trapped electrons of the defect transfer to the adsorbate and thus activate it. However, we have shown with our embedded-cluster approach that the neutral oxygen vacancy is not necessarily the dominant species, which has implications when interpreting results for future catalytic applications.

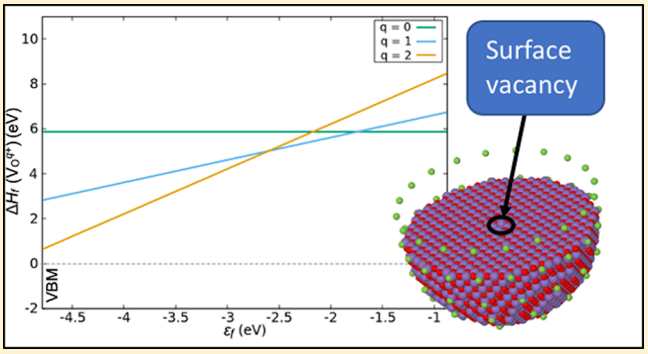

1. INTRODUCTION

Understanding the properties and stability of material defects is key in order to maximize the impact of materials engineering. Rock salt metal oxides are ideal test systems when studying how defects alter fundamental physico-chemical behavior,[1−4] with their stability also making them particularly appealing for applications that do not involve ambient conditions, such as heterogeneous catalysis.[5−8] In particular, rock salt oxides formed from early group 2 alkaline earth metals (Mg, Ca) have been extensively studied, both with respect to their defect structure and properties[9] and with the focus on potential applications in the catalytic transformation of CO_2.[10,11] In these investigations, computational methods lend themselves to investigating both the viability of reaction mechanisms as well as the large compositional search space for novel materials, with systematic investigations establishing a new standard when looking for beneficial material characteristics.[12,13] Computational screening of this nature was recently used to examine CO_2 adsorption on a variety of rock salt (100) surfaces, showing strong surface−adsorbate interactions and charge transfer for a range of materials.[14] One material that plays an important role in these studies is MnO, which is typically considered as a supporting material or a reaction promoter, rather than an active part of catalytic processes, due to its variable oxidation state;[15−19] in this highlighted work, however, MnO was identified as being reactive toward CO and CO_2.[18,19] This is perhaps unsurprising given that MnO can be prepared by thermal decomposition of $MnCO_3$,[20,21] which is done in an anaerobic environment to prevent the formation of higher oxidation state compounds. Observations of chemical reactivity are not without precedent for MnO: concerted effort has been applied toward characterizing the electronic properties of MnO-ZnO mixtures due to hypothesized photocatalytic capabilities.[22−27] It has also recently been of interest to tune catalytic properties by introducing individual defects, intrinsic or extrinsic,[1,6,28−32] to the oxide framework; such materials

Special Issue: Hans-Joachim Freund and Joachim Sauer Festschrift

Received: August 12, 2018
Revised: November 1, 2018
Published: November 14, 2018

have the stability of the host material while displaying novel catalytic chemistry. An example application of this nature is CO_2 adsorption over the (100) surface of Mn-doped MgO, with and without neighboring anion vacancies. The results showed that the multivalent Mn caused chemical bonding between the support and the adsorbate that was not present for undoped-MgO,[33] which complements experimental observations for mixed Fe-MnO/MgO catalysts as being reactive for the formation of light olefins from syngas.[17]

In this work, we have performed calculations to investigate the defect energetics in the bulk and at the (100) surface of MnO, and also investigated the surface reactivity. Defects, both intrinsic and extrinsic, are key for controlling the chemical properties of catalytic materials and optimizing surface reactivity. However, one of the complexities when investigating magnetic materials like MnO is the effect of temperature on the spin configuration. At room temperature, MnO is paramagnetic (PM) and adopts a cubic structure with lattice constant (a) of 4.445 Å,[34−36] but MnO has a Neél temperature (T_N) of 118 K,[37] below which it adopts an antiferromagnetic spin-configuration (AFM) with the d^5 valence electrons alternating in their spin alignment between nearest neighbor Mn^{2+} cations. In the case of MnO, the lowest energy AFM arrangement is with the spin aligned in a principal diagonal plane through the crystal [AFM(II)], rather than in the lowest-index (100), (010) or (001) plane [AFM(I)].[37,38] Calculations have confirmed this energetic ordering of spin configurations, with the ferromagnetic (FM) arrangement shown as higher in energy than either AFM option.[39−44] The AFM(II) spin-configuration is associated with a rhombohedral distortion to the unit cell: the experimental lattice constant, a, is 4.43015−4.4316 Å, and the unit cell angle, α, is 90.60−90.62°.[45−47]

In the following sections, we outline our method and results, focusing on the low-energy AFM(II) spin-configuration due to its highest relative stability in athermal conditions as these are the implicit conditions of a static quantum mechanical calculation. We introduce our chosen methodology, hybrid quantum- and molecular-mechanics, and we then investigate the electronic and energetic properties of defects in bulk MnO, providing new insight into the bulk properties of this material. We complement these calculations with an investigation of surface atomic vacancies at the low-energy (100) surface, and finally we test the reactivity of CO_2 over both pristine and defective MnO (100) surfaces.

2. COMPUTATIONAL METHODOLOGY

Calculations were performed using the additive hybrid quantum- and molecular-mechanical (QM/MM) embedded-cluster methodology, as realized in the ChemShell software package.[48,49] QM and MM energy evaluations were outsourced to the NWChem[50] and GULP[51−53] software packages, respectively, and geometry optimizations coordinated by the DL-FIND library.[54] The accuracy of this method has been previously shown for the study of intrinsic and extrinsic defects in bulk and surface environments of ionic oxides like MgO,[55,56] TiO_2,[57−59] In_2O_3, SnO_2, and ZnO.[60] The strength of the QM/MM embedded-cluster approach is that it allows the affordable use of hybrid-DFT, which is necessary for localizing defects and accurately predicting energetics. The power of this approach toward the accurate modeling of reaction processes is well illustrated previously by the work of Sauer et al.[61] Additionally, an aperiodic embedded-cluster model allows us to access an unambiguous reference state, namely the vacuum level (0 V), and also allows the facile study of charged defects, both bulk and surface, with the latter being extremely difficult to perform using periodic models.[62,63]

In this work, the bulk (surface) QM/MM embedded-cluster model is spherical (hemispherical) and has a radius of 30 Å. This results in a model that contains ∼10000 (∼5500) atoms. Within these (hemi)spherical clusters, the models are partitioned into QM and MM regions, where we define an inner "active" region that encompasses the central QM and MM atoms, which has a radius of 15 Å. This choice of size is based on our previous experiences modeling charged defects in MgO and noting the relatively local nature of geometric changes.[33] In total, the "active" regions contain ∼1300 and ∼600 atoms for bulk and surfaces, respectively. In the bulk (surface) models, the central 33 (23) atoms were represented using QM, with all remaining atoms represented using MM interactions. The atoms in the "active" region are able to move during geometry optimization, with an outer "frozen" region to ensure long-range bulk structure. The "frozen" region is 15 Å thick, which is chosen so as to be greater than the force field cutoff and thus ensure there are no energy discontinuities in the MM energy term. Additionally embedding the entire model is a series of point charges, with their values fitted to reproduce the long-range bulk electrostatic environment for the central "active" region, to an accuracy of 10^{-3} V. During geometry optimization, convergence is deemed complete when the residual forces are lower than 0.015 eV/Å.

For the MM calculations, the energy is calculated using a polarizable-shell interatomic force field (FF), which has Coulomb (E_{MM}^{Coul}), Buckingham (E_{MM}^{Buck}), and spring (E_{MM}^{spring}) terms, defined as:[52]

$$E_{MM}^{Coul} = k_e \frac{q_i q_j}{r_{ij}} \tag{1}$$

$$E_{MM}^{Buck} = A e^{-r_{ij}/\rho} - \frac{C}{r_{ij}^6} \tag{2}$$

$$E_{MM}^{spring} = \frac{1}{2} k_2 r_{ij}^2 \tag{3}$$

between two centers with indices i and j, separated by a distance r_{ij}. The FF parameters are the charge (q, in e), the spring constant (k_2, in eV Å^{-2}), and the Buckingham potential parameters A (eV), ρ (Å) and C (Å^6 eV); and k_e is Coloumb's constant. Our work builds on the FF parametrization of Lewis and Catlow (Table 1),[64] which gives an MnO lattice parameter (a) of 4.44 Å that matches experiment (4.45 Å) for the room temperature, cubic, PM MnO.[34−36] However, this FF does not reproduce the low-temperature AFM(II) rhombohedral unit cell, which is required to prevent unphysical strain occurring from a structural match between the QM and MM regions at the QM/MM interface. As a remedy, a Lennard-Jones potential (E_{MM}^{LJ}), taking the form of:

$$E_{MM}^{LJ} = -\frac{C_6}{r_{ij}^6} \tag{4}$$

was introduced between nearest neighbor Mn^{2+} cations with opposing spin by using a short-range cutoff of 5 Å to include nearest and next-nearest neighbor Mn−Mn interactions. This implementation mimics the attractive exchange interactions between antiparallel spins, with the Buckingham potential continuing to provide short-range repulsion. The C_6 parameter,

DOI: 10.1021/acs.jpcc.8b07846
J. Phys. Chem. C 2019, 123, 8133−8144

Table 1. Force Field Parameters for the MnO Calculations.[64] [a]

Coul. and spring	q_{core}	q_{shell}		k_2
Mn	−1.420	3.420		95.00
O	1.000	−3.000		54.76
Buck.	A	ρ	C	r_c
$Mn_{shell} - O_{shell}$	1007.4	0.3262	0.0	12.0
$O_{shell} - O_{shell}$	22764.3	0.1490	23.0	12.0
LJ		C_6		r_c
$Mn_{core}^{\uparrow\uparrow\uparrow\uparrow\uparrow} - Mn_{core}^{\downarrow\downarrow\downarrow\downarrow\downarrow}$		52.5		5.0

[a]Coul., Buck., and LJ are abbreviations/acronyms for Coulomb, Buckingham and Lennard-Jones, respectively. The parameters are the core charge (q_{core}, in e), the shell charge (q_{shell}, in e), the spring constants (k_2, in eV Å^{-2}), the Buckingham potential parameters A (in eV), ρ (in Å), C, the Lennard-Jones C_6 parameter, in units of Å^6 eV, and the cutoff for the different potentials (r_c) in Å.

which has units of Å^6 eV, was fitted in order to reproduce the low-temperature structure of the AFM(II) MnO phase (a = 4.43 Å, α = 90.6°).[45−47]

For the QM calculations, hydrid density functional theory (hybrid-DFT) was used with the B3LYP[65−67] and B97-3[68] exchange-correlation (XC) functionals. Results obtained with B3LYP provide a direct comparison with previous work on MgO, while B97-3 is a more advanced XC functional that has been fitted to a more extensive thermochemical data set. A Def2 triple-ζ valence plus polarization (TZVP) basis set was used for oxygen and carbon,[69] and a Stuttgart/Dresden relativistic small-core effective core potential (ECP), with modified basis sets, was used for Mn:[70] the most diffuse functions were removed to prevent artificial spread of electron density outside the QM region (edited basis set provided in the Supporting Information).[33,55] At the boundary of the QM region, it is typical to have cation-centered large-core ECPs to contain the electron density; however, no such ECPs have been derived for Mn^{2+}. Given the similar ionic radii of Mg^{2+} and Mn^{2+}, it was decided that large-core Mg^{2+} ECPs would be placed at the QM/MM boundary, with such an approach proving successful in a previous investigation of optical transitions for cubic-structured, FM- and AFM-ordered, MnO.[23]

3. BULK

3.1. Pristine. A bulk model of MnO was cut from the FF-optimized AFM(II) crystal structure. The QM/MM cluster was centered on the atomic species of interest: the O-centered model contains 14 Mn and 19 O atoms (Figure 1), whereas the Mn-centered model contains 14 O and 19 Mn atoms. Previous work has shown a model of this size is optimal as it ensures the QM region is large enough not to exhibit quantum confinement effects, which may occur due to the localized nature of the occupied states, while also not being excessively large so as to make calculations prohibitively expensive.[33,55,56] We also note here that stoichiometry is not a requirement for the QM region in the QM/MM embedded-cluster approach.[55−60] After geometry optimization, the AFM(II) electronic structure was preserved in both models, with Mulliken analysis showing an average spin density of 4.8 e on each Mn^{2+} cation when using either XC functional, in agreement with experiment;[71] however, the geometric structure is noted as being slightly distorted. For both the B3LYP and B97-3 O-centered models of pristine MnO, the

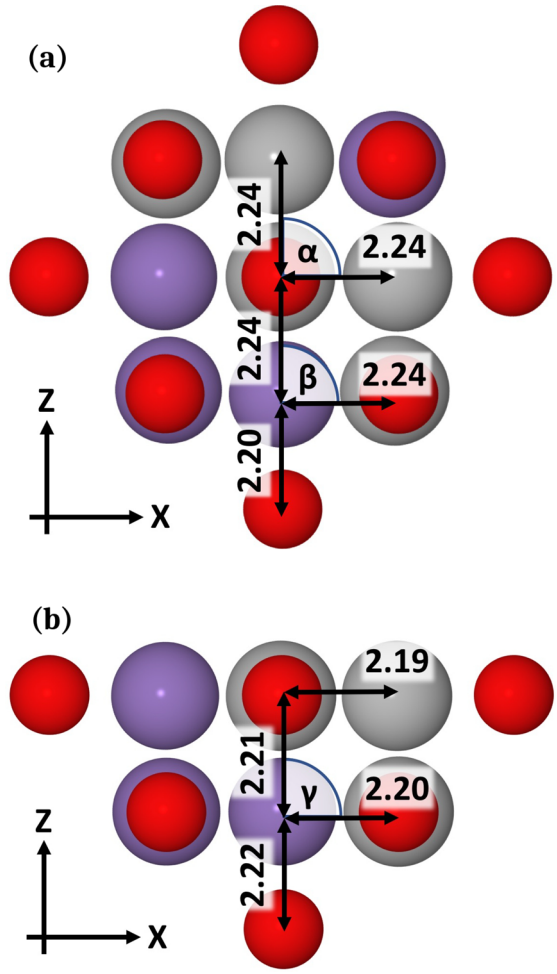

Figure 1. Structures of the QM region in the QM/MM models of the B3LYP-optimized (a) bulk and (b) surface models, as viewed with a cutplane through the x- and z-axes. Purple and gray spheres represent Mn atoms with spin-up and spin-down configurations, respectively, and red spheres represent oxygen atoms. Bond lengths are given in Å, and the denoted angles α, β, and γ are 90.6, 90.6, and 90.4°, respectively.

mean bond distances in the QM region stay constant at 2.21 Å but in a range of 2.16−2.24 Å, with bond lengths longer in the center of the QM region. Mean bond distances across the QM/MM boundary contracted (expanded) slightly for O_{QM}−Mn_{MM} (Mn_{QM}−O_{MM}) interactions, with averages of 2.18 and 2.24 ± 0.01 Å, respectively. Central bond angles were unaltered (α = 90.6°). These results were compared with geometry optimization of a range of QM/MM models with 7, 19, 27, 33, 45, 57, 63, 75, and 81 atoms in the QM region. It is noted that average bond length within the QM region and across the QM/MM boundary remains relatively constant (±0.01 Å), with the exception of the Mn_{QM}−O_{MM} interaction for which 2.24 Å is large compared to the more common observation of 2.21−2.22 Å. Interestingly, the range of bond lengths for those intersecting the QM/MM boundary (and in the MM region) remains stable, whereas within the QM region the range increases up to 2.17−2.27 Å for the 81-atom QM region, which also results in significant distortion of the bond angles. For the Mn-centered clusters, the distances between central and nearest neighbor atoms also increased, up to 2.25 Å; however, bond lengths in the QM region toward the boundary contracted significantly (2.15 Å). This contraction

DOI: 10.1021/acs.jpcc.8b07846
J. Phys. Chem. C 2019, 123, 8133−8144

led to inversion of the bond angle in some cases, with variation between 89.0 and 90.7°. While these observations are indicative of a slight force mismatch between the QM and MM regions, the structural changes do not adversely affect energetics, as discussed subsequently in our analysis.

The energetic position of the valence band maximum (VBM) can be calculated by simulating the ionization of an electron from the bulk environment in to vacuum, as

$$MnO^0 \rightarrow MnO^+ + e^- \quad (5)$$

The energy of an electron far removed from the bulk (i.e., at the vacuum level) is 0 eV, and so the vertical ionization energy (I_v) is

$$I_v = E(MnO^+) - E(MnO^0) \quad (6)$$

As well as I_v, which represents the instantaneous process of removing an electron, one can subsequently calculate the stabilization of a hole state as the adiabatic ionization (I_a). For both I_v and I_a, the starting structure is that of optimized MnO^0: the nuclear coordinates are frozen for I_v, allowing only the electronic configuration (and MM shells) to optimize, making this the appropriate method to place the VBM, whereas the nuclear centers are free to move for the I_a, the energy of which could be compared to emission spectra. We note that for $E(MnO^+)$, and any other charged QM/MM cluster, the *a posteriori* long-range dielectric correction of Jost is included in the total energy to compensate for the finite size of the polarizable region in our QM/MM model.[33,72,73]

For the O-centered clusters, which we will focus on throughout our work, I_v and I_a are 4.79 (5.14) eV and 3.46 (3.68) eV, respectively, when using the B3LYP (B97-3) XC functional; for the Mn-centered clusters, I_v is 4.76 (5.07) eV for the same XC functionals. The similarity in I_v between our two model configurations gives us significant confidence in the ability to compare the results of our calculations. To further clarify the error bar in our approach, we also calculated I_v for the O-centered cluster when varying the size of the QM region between 7, 19, 27, 33, 45, 57, and 63 atoms. The B3LYP calculated values, which were respectively 5.43, 4.63, 4.85, 4.79, 4.76, 4.75, and 4.77 eV, vary significantly at small sizes, due to quantum confinement effects, but converge to within 0.04 eV for sizes of 33 atoms and greater. This similarity is particularly noteworthy given the structural differences of the respective QM regions, as highlighted above, when changing the QM region size. Overall, we can combine the highlighted differences to present a conservative compound error bar of ±0.1 eV on our results. While previous calculations of I_v for bulk MnO are unavailable, calculated position of the VBM at surfaces have been presented in the range of 4.5−5.5 eV (discussed further in section 4);[12,13] however, we also note that the only available experimental data, taken from photoelectrochemical measurements of PM MnO, shows I_v to be considerably greater as 7.09 eV.[74] This discrepancy between experiment and theory could be related to the differences in magnetic and structural configuration, though neither effect results typically in such significant deviations; therefore, the difference is perhaps more likely due to experimental error and/or DFT methodological choices. Tests show that the ionization potential of gas-phase Mn atoms match experiment (7.43 eV in experiment,[75] 7.64 eV with B3LYP), but ligand-field interactions result in splitting of degenerate levels within the bulk materials: an underestimation of I_v with DFT XC functionals has been previously observed for bulk materials and should be remembered when considering the position of both conduction band (CB) and valence band (VB) edges.[55] Previous literature tells us the VBM is of mixed nature in AFM(II) MnO, with PBE0 giving a 25/75% split between O 2p- and Mn 3d-states, respectively;[41] in our calculations, Mulliken analysis on both the O-centered and Mn-centered models shows that the electron is removed from the Mn valence shells when forming MnO^+, hence the good agreement between the two models, and the remaining hole localizes on an Mn atom during subsequent geometry relaxation.

The discrete nature of the QM region in the QM/MM cluster, and the resulting quantum confinement, results in a poor representation of the CB and an overestimation of the band gap, E_g; therefore, bulk E_g has been taken from literature to position the conduction band minimum (CBM). Experimental reports of E_g are for the room temperature, PM ordering, and range between 3.6 and 4.9 eV;[76−78] calculated band gaps of 2.9−4.02 eV and 3.5−4.2 eV have been presented for AFM(II) MnO from hybrid-DFT[40−42] and GW[12,79,80] calculations. In this work, we have taken the result of E_g for the B3LYP XC functional (3.92 eV) as this exactly matches one of our XC functionals;[40] thus, we position the CBM of AFM(II) MnO using the I_v from our O-centered clusters, obtaining −0.87 (−1.22) eV relative to the vacuum level when using the B3LYP (B97-3) XC functionals.

3.2. Intrinsic Defects. In order to illustrate the capabilities of the embedded-cluster QM/MM approach, we have calculated the defect formation energy for neutral and charged vacancies in MnO, as well as the energy levels of trapped electrons/holes at the remaining vacancies. A Kröger−Vink defect notation is used. A neutral cation vacancy may be considered as forming thus

$$Mn^x_{Mn} \rightarrow V^x_{Mn} + Mn^x_{ref} \quad (7)$$

with a formation energy of

$$\Delta H_f(V^x_{Mn}) = E(V^x_{Mn}) + E(Mn^x_{ref}) - E(Mn^x_{Mn}) \quad (8)$$

The energy of the reference states, $E(Mn^x_{ref})$, is defined as $E(Mn_{at}) + \mu(Mn)$, where $E(Mn_{at})$ is the calculated energy of the gas-phase atom and $\mu(Mn)$ is the chemical potential of Mn. Here, $E(Mn_{at})$ was calculated as $E(Mn_{at}^{2+})$ minus the first and second experimental ionization energies, as successfully applied previously for embedded-cluster calculations with modified basis sets.[33,81] Ideally, $\mu(Mn)$ would also be calculated at the same level of theory as our QM/MM calculations of MnO, which in turn requires calculating ΔH_f (Mn), i.e., the energy of bulk Mn; however, due to the weakness in hybrid-DFTs at representing delocalized states in metallic systems, we found ΔH_f (Mn) to be underestimated by >1 eV when using hybrid-DFT (see the Supporting Information). This inability to accurately model transition metals is not isolated to our particular choices of hybrid DFT exchange-correlation functionals, but a more general problem for the field as highlighted by Janthon et al.[82] Thus, in order to minimize the impact of these inaccurate hybrid-DFT models for bulk Mn, the experimental ΔH_f was used for the reference states of Mn and MnO, and only ΔH_f (O_2) was calculated to acquire $\mu(Mn)$; from this, the respective products in high- and low-partial pressures of O_2, $p(O_2)$, are MnO(s) [ΔH_f (MnO) − $\frac{1}{2}\Delta H_f$ (O_2) = −126.3 kJ mol^{-1}] and Mn(s) [ΔH_f (Mn) = −279.58 kJ mol^{-1}].[37,83] For the equivalent calculation of O_2 vacancies in high- and low-$p(O_2)$, the reference states are O_2

DOI: 10.1021/acs.jpcc.8b07846
J. Phys. Chem. C 2019, 123, 8133−8144

(g) [$\frac{1}{2}\Delta H_f$ (O_2) = −258.90 kJ mol^{-1} using B3LYP and −261.67 kJ mol^{-1} using B97-3] and MnO (s) [ΔH_f (MnO) - ΔH_f (Mn) = −105.62 kJ mol^{-1}],[37,83] respectively.

If a given vacancy forms in a charged state, the energy associated with adding/removing an electron must be included. The Fermi Level (ϵ_f) is a common source of electrons and holes in traditional semiconductors, depending on its positioning, and its inclusion in our calculations makes ΔH_f:

$$\Delta H_f(V_{Mn}^q) = E(V_{Mn}^q) + E(Mn_{ref}^x) - E(Mn_{Mn}^x) - q\epsilon_f \quad (9)$$

Both positive and negative values of the charge, q, are feasible: in the case of $q < 0$, electrons are taken from the Fermi Level and thus $-q\epsilon_f$ is positive to reflect the energy required for this abstraction; in the case of $q > 0$, electrons are transferred to the Fermi level; thus, there is an energy gain. For an oxygen vacancy, the enthalpy of formation is similarly:

$$\Delta H_f = E(V_O^q) + E(O_{ref}^x) - E(O_O^x) - q\epsilon_f \quad (10)$$

An alternative charge compensation is the formation of Schottky defect pairs, which are prevalent in wide band gap materials,[84] whereby the charge on a cation vacancy is compensated by an opposing charge on an anion vacancy. For a pair of double-charged vacancies, this is

$$Mn_{Mn}^x + O_O^x \rightarrow V_{Mn}'' + Mn_{at}^{\bullet\bullet} + V_O^{\bullet\bullet} + O_{at}'' \quad (11)$$

$$\rightarrow V_{Mn}'' + V_O^{\bullet\bullet} + MnO(s) \quad (12)$$

with the recombination of the charged ions in eq 11 leading to the reformation of MnO(s) in eq 12. In this case, ΔH_f for the Schottky defect is

$$\Delta H_f(V_{Mn}'' + V_O^{\bullet\bullet}) = E(V_{Mn}'') + E(V_O^{\bullet\bullet}) + E[MnO(s)] - E(Mn_{Mn}^x) - E(O_O^x) \quad (13)$$

where we calculate E[MnO(s)] as

$$E[MnO(s)] = E(Mn_{at}^x) + \Delta H_f(Mn) + E(O_{at}^x) + \frac{1}{2}\Delta H_f(O_2) + \Delta H_f[MnO(s)] \quad (14)$$

B3LYP-calculated defect formation energies are presented in Figure 2 for the atomic vacancies. For O vacancies, calculated with the O-centered model, $V_O^{\bullet\bullet}$ is the most stable at low ϵ_f, with the neutral V_O^x defect preferred as ϵ_f tends toward ϵ_{CBM}; however, the V_O defects are only more favorable than V_{Mn} under high-$p(O_2)$ when ϵ_f is in the lower half of the band gap. The neutral and negatively charged V_O defects show little disruption of the perfect bulk structure, with minimal atomic displacements. Mulliken analysis shows the two electrons (e′) freed when forming the V_O^x defect would be trapped in the vacancy, forming an F-center, with an F^+-center also stable when one of the defect electrons has been removed i.e. a $V_O^{\bullet}$ defect. Unsurprisingly, negatively charged V_O sites (V_O' and V_O'') are unstable at all values of ϵ_f.

For Mn vacancies, calculated with the Mn-centered model, ΔH_f decreases with q when $\epsilon_f = \epsilon_{CBM}$, and increases with q when $\epsilon_f = \epsilon_{VBM}$: this shows that the defects would donate electrons when ϵ_f is low (large energy gain) and accept electrons when ϵ_f is high (small energy cost). For the B3LYP XC functional, we calculate that ΔH_f (V_{Mn}'') is exothermic

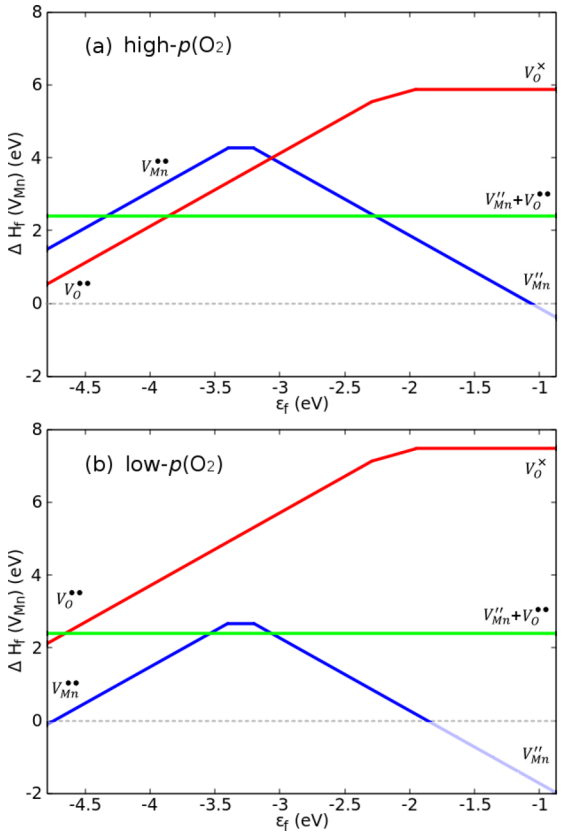

Figure 2. ΔH_f as a function of ϵ_f for V_{Mn}, V_O, and Schottky defects, given in blue, red and green, respectively, calculated using the B3LYP XC functional for (a) high- and (b) low-$p(O_2)$ conditions. Only the lowest energy defect, of any given type, is marked at any given value of ϵ_f; full graphs of all values of ΔH_f, for all values of q, are provided in the Supporting Information. The minimum and maximum of ϵ_f on the x-axis represents the band edges for the valence and conduction band, respectively. The 0 eV line on the y-axis, splitting endo- and exothermic processes, is marked by a gray dashed line; ΔH_f values below 0 eV are physically infeasible and thus given in a pale color.

when $\epsilon_f = \epsilon_{CBM}$ at both low- and high-$p(O_2)$; we note that n-type conditions of ϵ_f would require an excess of electrons generated from e.g. oxygen vacancies. In previous literature, n-type conditions have more commonly been considered: Aschauer et al. presented results from periodic PBESol+U calculations with ϵ_f positioned 2.8 eV above the VBM, i.e. toward the CBM, and found that ΔH_f (V_{Mn}'') was 1.5 eV lower than ΔH_f (V_{Mn}'), which in turn was 1.7 eV more preferable than ΔH_f (V_{Mn}^x); they also reported ΔH_f ($V_O^{\bullet\bullet}$) as 4.5 eV higher in energy than ΔH_f (V_{Mn}'').[85] These observations are in agreement with our results, with the same ϵ_f positioning giving respective differences between ΔH_f (V_{Mn}''), ΔH_f (V_{Mn}') and ΔH_f (V_{Mn}^x) of 1.27 and 1.13 eV (Figure S1, Supporting Information), and between ΔH_f (V_{Mn}'') and ΔH_f ($V_O^{\bullet\bullet}$) of 4.26 (7.45) eV for high (low)-$p(O_2)$. Previous experimental work focuses on the dominant Mn vacancy at varying high temperatures ($T > 1000$ K), the modeling of which is beyond the scope of this work, but generally notes the prevalence of V_{Mn}'.[86]

As the VBM is lower at −5.14 eV for B97-3, we observe that both ΔH_f (V_{Mn}'') and ΔH_f ($V_{Mn}^{\bullet\bullet}$) are exothermic for $\epsilon_f = \epsilon_{CBM}$ and ϵ_{VBM}, respectively, under low-$p(O_2)$ conditions. At both high and low values of ϵ_f, the transition from endothermic to exothermic for ΔH_f indicates the limit for ϵ_f in this material as,

DOI: 10.1021/acs.jpcc.8b07846
J. Phys. Chem. C 2019, 123, 8133−8144

in the exothermic regime, the material properties would change due to the propensity for defect formation. Thermodynamic stability regimes for the singly charged V'_{Mn} and $V^{\bullet}_{Mn}$ defects are not observed for either B3LYP or B97-3.

Structurally, V''_{Mn} formation results in expansion around the vacant site, with contraction of Mn−O bonds between neighboring atoms to compensate for the lost coordination. For the B3LYP optimized model, Mn−O bonds around the V''_{Mn} defect are 2.12−2.14 Å, in agreement with Aschauer et al., who report bond lengths of 2.11 Å,[85] while we observe shorter bonds of ∼2.01 Å for bonds between O atoms neighboring the defect and Mn atoms at the edge of the QM region. As the charge of QM region is reduced (i.e., electrons are removed), much shorter Mn−O bonds are observed: for V'_{Mn} there is a shorter bond of 1.98 Å; for V^{x}_{Mn}, two bonds of 1.81 and 1.88 Å are observed; for $V^{\bullet}_{Mn}$ there is an additional bond of 1.98 Å; and for $V^{\bullet\bullet}_{Mn}$, four bonds of between 1.81 and 1.88 Å are calculated. These shorter bonds are all indicative of Mn−O bond lengths after the oxidation of Mn^{2+} to Mn^{3+},[42,85,87] with Aschauer et al. reporting distances of 1.92 Å for the PBESol+U approach. For B97-3, similar structural observations are made, except that for V'_{Mn} and $V^{\bullet}_{Mn}$ the short bonds are all below 1.86 Å; however, this geometric difference does not appear to influence the defect energetics as neither of the singly charged defects are stable with either XC functional. Mulliken spin analysis shows that the holes ($h^{\bullet}$) created by removing a lattice Mn cation localize on nearest neighbor Mn sites, forming Mn^{3+} cations ($Mn^{\bullet}_{Mn}$), which is consistent for V'_{Mn} through to $V^{\bullet\bullet}_{Mn}$. Additionally, via a comparison of states of different multiplicity and Mulliken spin analysis, we observe that the singly charged defects of V'_{Mn} and $V^{\bullet}_{Mn}$ are >1.5 eV more stable when the defect electron aligns with the d^5 valence electrons of the removed Mn atom, i.e. in agreement with the AFM(II) configuration.

In general, MnO is characterized by experiment as a p-type material (i.e., rich in $h^{\bullet}$ charge carriers) due to Mn vacancies caused by an excess of oxygen, with investigations having been performed exclusively at room temperature or higher; thus considering cubic, paramagnetic MnO.[35,88,89] O'Keeffe et al. stated that the majority defects in their samples were V''_{Mn}, with charge compensation via two $Mn^{\bullet}_{Mn}$ centers and $^1/_2O_2$ (g);[35] in our calculations, Mulliken analysis shows that multiple $Mn^{\bullet}_{Mn}$ defects are the preferred stabilizer for all V_{Mn} defects, but the formation enthalpies imply that V''_{Mn} would only form with ϵ_f positioned midgap or higher (Figure 2). Our results for low-$p(O_2)$ agree with expectation of V_{Mn} being most stable; for high-$p(O_2)$, our calculations show competition between the $V^{\bullet\bullet}_{O}$ and $V^{\bullet\bullet}_{Mn}$ defects at low ϵ_f, which would be shifted to further favor $V^{\bullet\bullet}_{O}$ if we were to consider an MnO_2 (s) reference state, which is most likely at high-$p(O_2)$: $\mu(Mn) = -2.2$ kJ mol^{-1} i.e. the ΔH_f (V_{Mn}) line would be shifted further upward.[37,83] A possible source of this difference is the temperature and phase of the MnO in our work, although we also suggest that a lack of long-distance exchange coupling may have affected the V_{Mn} calculations, which could possibly be rectified by consideration of a larger QM region. Overall, the presence of a stability window for e′ charge carriers is in agreement with (high temperature) Hall measurements that show the existence of e′ charge carriers with higher mobility than $h^{\bullet}$ at low-$p(O_2)$.[88,90−92]

We present ΔH_f for vacancy defects in Table 2, compared with ϵ_f-compensated defects in their most favored conditions, i.e. elemental products, when ϵ_f is equal to the midgap branch point. As shown in eq 13, Schottky defects are mutually cooperative as holes and electrons recombine. Our results show that a Schottky defect with Mn^{2+}/O^{2-} pairings are energetically most favorable. By summing ΔH_f for the charge-carrier-compensated vacancies and comparing to the formation energy of Schottky defects, we also see that, when ϵ_f is positioned midgap or higher (i.e., n-type), this Schottky defect is more favorable than all possible combinations of charge-carrier-compensated defects; however, in general the *individual* ϵ_f-compensated defects remain energetically more preferable. Experimentally, Schottky defects were considered previously by Crevecoeur and de Wit in order to explain conductivity measurements;[91] however, further work by Pai and Honig concluded that a two-carrier model in MnO is very unlikely.[92] As an additional note, we see in Table 2 that the most stable V_{Mn} defects differ between the B3LYP and B97-3 XC functionals at the midgap point. This difference occurs because of the larger I_v when using B97-3 (5.14 eV) compared to B3LYP (4.79 eV), which in turn lowers the energy of the midgap point and favors the loss of e′ charge carriers more when using B97-3 than with B3LYP.

The energy levels of electrons trapped at defect sites are presented in Figure 3. Here, the ΔSCF method (analogous to

Table 2. Formation Enthalpy (eV) When Using the B3LYP (B97-3) XC Exchange-Correlation Functional for Various Defects, both Atomic Vacancies and Combined Schottky-Type, in a Variety of Charge States When the Fermi Level Is Positioned Mid Band Gap, i.e., Equidistant from Valence and Conduction Band Edges[a]

defect reactions	ΔH_f (eV)
oxygen vacancy, low-$p(O_2)$	
$O^{x}_{O} \rightarrow V''_{O} + 2h^{\bullet\bullet} + MnO(s)$	12.84 (13.63)
$O^{x}_{O} \rightarrow V'_{O} + h^{\bullet} + MnO(s)$	10.07 (10.29)
$O^{x}_{O} \rightarrow V^{x}_{O} + MnO(s)$	7.47 (7.17)
$O^{x}_{O} \rightarrow V^{\bullet}_{O} + e' + MnO(s)$	6.58 (6.13)
$O^{x}_{O} \rightarrow V^{\bullet\bullet}_{O} + 2e' + MnO(s)$	6.03 (5.40)
oxygen vacancy, high-$p(O_2)$	
$O^{x}_{O} \rightarrow V''_{O} + 2h^{\bullet\bullet} + {}^1/_2O_2(g)$	11.25 (12.04)
$O^{x}_{O} \rightarrow V'_{O} + h^{\bullet} + {}^1/_2O_2(g)$	8.48 (8.70)
$O^{x}_{O} \rightarrow V^{x}_{O} + {}^1/_2O_2(g)$	5.88 (5.58)
$O^{x}_{O} \rightarrow V^{\bullet}_{O} + e' + {}^1/_2O_2(g)$	4.99 (4.54)
$O^{x}_{O} \rightarrow V^{\bullet\bullet}_{O} + 2e' + {}^1/_2O_2(g)$	4.44 (3.81)
manganese vacancy, low-$p(O_2)$	
$Mn^{x}_{Mn} \rightarrow V''_{Mn} + 2h^{\bullet} + Mn(s)$	1.95 (2.76)
$Mn^{x}_{Mn} \rightarrow V'_{Mn} + h^{\bullet} + Mn(s)$	2.38 (2.92)
$Mn^{x}_{Mn} \rightarrow V^{x}_{Mn} + Mn(s)$	2.67 (2.74)
$Mn^{x}_{Mn} \rightarrow V^{\bullet}_{Mn} + e' + Mn(s)$	3.35 (3.10)
$Mn^{x}_{Mn} \rightarrow V^{\bullet\bullet}_{Mn} + 2e' + Mn(s)$	3.81 (3.11)
manganese vacancy, high-$p(O_2)$	
$Mn^{x}_{Mn} \rightarrow V''_{Mn} + 2h^{\bullet} + MnO(s)$	3.54 (4.35)
$Mn^{x}_{Mn} \rightarrow V'_{Mn} + h^{\bullet} + MnO(s)$	3.97 (4.51)
$Mn^{x}_{Mn} \rightarrow V^{x}_{Mn} + MnO(s)$	4.26 (4.33)
$Mn^{x}_{Mn} \rightarrow V^{\bullet}_{Mn} + e' + MnO(s)$	4.94 (4.69)
$Mn^{x}_{Mn} \rightarrow V^{\bullet\bullet}_{Mn} + 2e' + MnO(s)$	5.40 (4.69)
Schottky pair	
$Mn^{x}_{Mn} + O^{x}_{O} \rightarrow V''_{Mn} + V^{\bullet\bullet}_{O} + MnO(s)$	2.40 (2.57)
$Mn^{x}_{Mn} + O^{x}_{O} \rightarrow V'_{Mn} + V^{\bullet}_{O} + MnO(s)$	3.38 (3.47)
$Mn^{x}_{Mn} + O^{x}_{O} \rightarrow V^{x}_{Mn} + V^{x}_{O} + MnO(s)$	4.56 (4.33)
$Mn^{x}_{Mn} + O^{x}_{O} \rightarrow V^{\bullet}_{Mn} + V'_{O} + MnO(s)$	7.84 (7.81)
$Mn^{x}_{Mn} + O^{x}_{O} \rightarrow V^{\bullet\bullet}_{Mn} + V''_{O} + MnO(s)$	11.07 (11.15)

[a]Holes and electrons are denoted as $h^{\bullet}$ and e′, respectively.

DOI: 10.1021/acs.jpcc.8b07846
J. Phys. Chem. C 2019, 123, 8133−8144

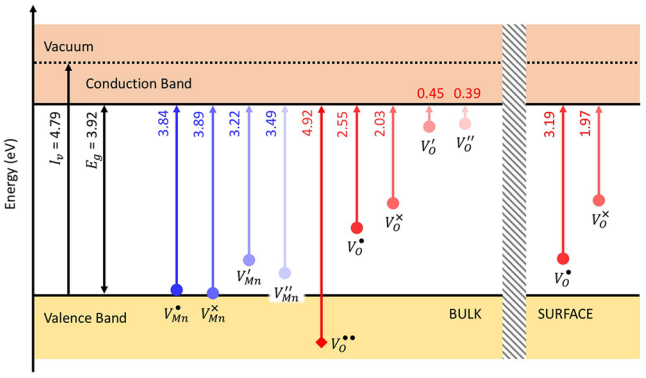

Figure 3. Pictorial representation of defect levels for neutral and charged lattice vacancies in the bulk (left) and at the surface (right) of MnO, as calculated using the B3LYP XC functional. All energies are in eV, with the valence (VB) and conduction band (CB) marked in gold and pink, respectively, and the vacuum level also marked with a dashed horizontal line, as defined by combining the ionization potential (I_v) and the energetic band gap (E_g). Mn and O vacancy levels are labeled and their distance from the CB is represented by blue and red arrows, respectively, with the color scheme matched to the equivalent charged systems in Figure 2; defect levels marked with circles are trap states in the band gap, while those marked with diamonds are resonant in the VB.

eq 6) was used to calculate the energy levels;[93] when coupled with values of I_v and E_g, one can determine the position of defects relative to the VBM and CBM. Starting with the Mn vacancies, the sites with two and one associated electrons (V''_{Mn} and V'_{Mn}, respectively) are mid band gap, as may be expected from the behavior of cation defects in similar materials e.g. V_{Mg} in MgO[94] and V_{Zn} in ZnO.[95] However, unlike V_{Zn}, neutral and positive V_{Mn} defects are positioned at the VBM. In the case of both V'_{Mn} and $V^{\bullet}_{Mn}$, it is noted that the electron energy levels are higher than defects with an extra electron, further consolidating our observation that these defects are unstable; similar results are observed for the B97-3, as shown in the Supporting Information, in agreement with our observations from Table 2. Such results are not observed for V_O, where V^{x}_{O} and $V^{\bullet}_{O}$ are positioned midgap, similar to the negatively charged Mn vacancies and the equivalent sites that have been well studied in MgO.[55,94] Negatively charged V_O sites are positioned very close to the CBM and are not expected to be stable.

4. (100) SURFACE

4.1. Pristine. The (100) surface is the most stable for MnO, as with many other rock salt oxides,[96] and it is considered here for reactivity investigations. A surface model was prepared at the MM level, using the AFM(II) configuration, with minor rumpling effects occurring such that the O atoms displaced 0.01 Å outward (0.5% change in bond lengths), relative to the Mn atoms, and the distance between the top-surface layer and subsurface layer contracted to 2.20 Å (0.5% change in interlayer distance). The results for rumpling are mixed in the previous literature, with MEIS[97] and LEED[98] giving inward and outward O displacement, respectively; likewise, computational results for the LDA XC functional give retraction of O from the surface,[99] while PBE and PBE+U give outward O displacement by 1.3−1.6%.[100] The results for interlayer contraction are more consistent within each method, yet contradictory between theory and experiment: MEIS and LEED indicate that the distance between surface and subsurface layers increases, by 0.1−1.1%,[97,98] whereas DFT gives interlayer contraction by 0.3−1.6%.[99,100] Our calculated displacements match previous computations well, and we note that the error bars on experiment are large compared to the values being considered.

A QM/MM model was constructed from our MM surface, centered on a surface oxygen atom; structural optimization resulted in atom displacements of only 0.01 Å (0.5%) compared to the MM model. The surface ionization potential was then calculated using eq 6, with both high- and low-spin configurations considered for the MnO^{+} surface: a high-spin configuration corresponds to ionization from the O 2p-orbitals, whereas the low-spin configuration corresponds to removing an electron from the Mn 3d-orbitals. Our calculations show that the highest occupied states (VBM) belong to the Mn 3d-orbitals, for which I_v is 4.77 (5.09) eV and I_a is 3.32 (3.52) eV when using the B3LYP (B97-3) XC functional, whereas the O 2p-states are marginally lower in energy with I_v = 4.95 (5.29) eV, for the same XC functionals. We note that our results for I_v and I_a are similar to bulk: for the favorable low spin ionization of the surface, I_v differs by <0.1 eV and I_a by <0.2 eV. Mulliken analysis shows that this similarity is because surface ionization removes an electron from a *subsurface*, rather than *surface*, Mn cation. Further calculations using constrained DFT, whereby the ionized electron is removed specifically from a surface atom, result in I_v = 5.06 and 5.43 eV for B3LYP and B97-3 XC functionals, respectively, which indicates the surface valence-band bending downward.

Motivated by these results, we also calculated second and third ionization energies for the MnO surface. It was noted that the lowest energy configurations for the vertical ionization of a second electron is with two Mn^{3+} cations positioned subsurface, forming a $[Mn^{3+}]_2$ complex, which is more stable than a Mn^{4+} positioned subsurface or on the surface; the respective energetic ordering is 5.65 (5.97) < 6.27 (6.72) < 6.45 (6.91) eV when using the B3LYP (B97-3) XC functional. The $[Mn^{3+}]_2$ configuration was also more favorable for I_a. Analogous to eq 9, we then looked at formation energies of the ionized surface defects, finding that Mn^{3+} through to Mn^{5+}, and combinations therein, would be exothermic as ϵ_f approaches the VBM; isolated occurences of Mn^{3+} are most favorable when considered per hole created: −1.46 (−1.57), −1.20 (−1.32) and −0.97 (−1.22) eV for single, double and triple Mn^{3+} defect coupling, when using the B3LYP (B97-3) XC functional. Again, we note that negative ΔH_f values indicate a physically unstable ϵ_f, as the material would spontaneously lose electrons; however, we emphasize the trend in stability of different defects. Compensating Mn vacancies were also considered, but found to be higher in energy than compensation via ϵ_f.

Our positioning of the VBM at the (100) surface is in good agreement with previous computations by Toroker et al. using hybrid-DFT methods, where a periodic slab model was used with a vacuum region and the electrostatic potential in the vacuum gap taken as the reference vacuum level. With this model, they obtained ϵ_{VBM} of −4.48, −4.96, −5.28, and −5.57 eV for the PBE+U, HSE, PBE0, and G0W0 (DFT+U) methods;[12] Stevanovic et al. used a similar technique to obtain I_v = 5.08 eV. However, neither our nor other authors' results match with the experimental estimates of −7.5 ± 0.8 eV, taken from photoelectron spectroscopy (PES) measurements by Fujimori et al.,[101] though these relate to the room temperature

DOI: 10.1021/acs.jpcc.8b07846
J. Phys. Chem. C 2019, 123, 8133−8144

PM phase. A position of the VB can also be implied from the PES-BIS (bremsstrahlung isochromate spectroscopy) measurements of van Elp et al., where the CBM was reported as being −3.6 ± 1.2 eV;[76] this again positions the VBM well below our estimates. The offset between experimental and computational results is worth remembering when interpreting our defect calculations: a lower value of ϵ_{VBM} stabilizes electrons, which will shift the equilibrium between ϵ_f-compensated charged defects such that positively charged defects will be more favored.

4.2. Intrinsic Defects. The formation energies of neutral and positively charged oxygen surface vacancies are presented in Figure 4. ΔH_f (V_O^x) is almost identical to the bulk at 5.88

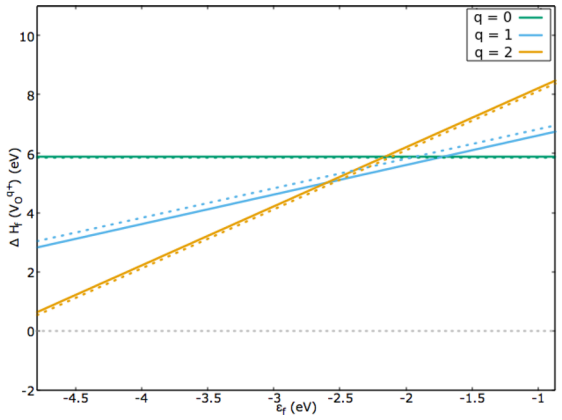

Figure 4. ΔH_f as a function of ϵ_f for V_O^{q+} in surface (solid) and bulk (dashed) environments, with charge q = 0 (green), 1 (blue) and 2 (yellow). The minimum and maximum of ϵ_f on the x-axis represents the band edges for the valence and conduction band, respectively. The 0 eV line on the y-axis, splitting endo- and exothermic processes, is marked by a gray dashed line.

(5.60) eV for the B3LYP (B97-3) XC functional, differing by only 0.02 eV. This difference relative to bulk increases ∼0.2 eV for $V_O^{\bullet}$, with ΔH_f ($V_O^{\bullet}$) = 2.81 (2.37) eV at the surface when considering $\epsilon_f = \epsilon_{VBM}$; for $V_O^{\bullet\bullet}$, ΔH_f ($V_O^{\bullet\bullet}$) is then almost identical for the surface and bulk, at 0.63 (−0.04) eV for the B3LYP (B97-3) XC functional. Analysis of the defect levels shows that, like the bulk, the favored spin configuration when ionizing to the $V_O^{\bullet}$ states is low-spin (LS): I_v^{LS} ($V_O^x \rightarrow V_O^{\bullet}$) = 2.84 eV compared to I_v^{HS} ($V_O^x \rightarrow V_O^{\bullet}$) = 3.13 eV for high-spin (HS) configurations, using the B3LYP XC functional. Also similar to the bulk, the structural integrity of the void is preserved, with neighboring bond distances remaining close to the bulk values. However, removing a second electron from the oxygen vacancy is more difficult: I_v ($V_O^{\bullet} \rightarrow V_O^{\bullet\bullet}$) and I_a ($V_O^{\bullet} \rightarrow V_O^{\bullet\bullet}$) are 4.06 (4.22) and 2.60 (2.73) eV, respectively, with the B3LYP (B97-3) XC functional, which is ∼0.6 eV larger than for the bulk. The structure of the defect remains relatively unchanged.

4.3. CO_2 Adsorption. Rock salt oxides have recently been proposed as candidate materials for the catalytic transformation of CO_2,[10,11,14] and here we investigate the initial step of that reaction: CO_2 surface adsorption. Previously, it has been shown that surface defects on MgO, specifically oxygen vacancies, can affect CO_2 adsorbate binding,[55] both structurally and energetically, which is further amplified by the presence of extrinsic cation dopants like Mn_{Mg}.[33] A favorable initial step involves charge transfer from the support to the CO_2, which results in bending of the linear CO_2, and this can be aided by high-energy defect levels associated with oxygen vacancies.

There are two possible orientations for a CO_2 molecule on the (100) surface: parallel or perpendicular to the surface xy-plane.[55] Downing et al. showed that, for pure MgO, parallel adsorption is stronger over the pristine surface, whereas perpendicular orientation is more favorable in the presence of V_O. In the case of MnO, parallel adsorption is again stronger over the pristine surface than perpendicular, with the C atom interacting with a surface oxygen (Figure 5) with an adsorption

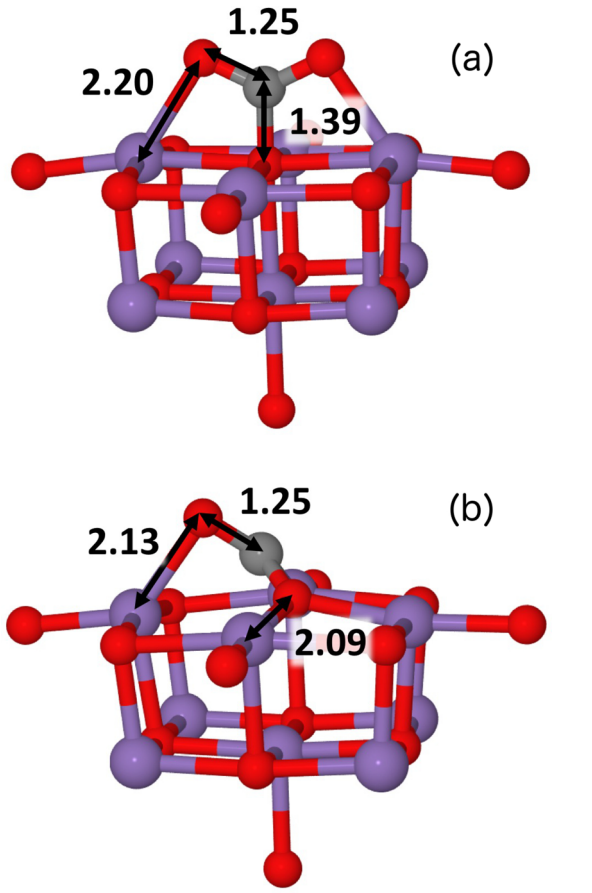

Figure 5. Structure of CO_2 adsorbed over: (a) a perfect (100) MnO surface and (b) a V_O^x defect at the structure surface. In the latter case, the CO_2 is seen to fill the oxygen vacancy. Red, purple, and gray spheres represent O, Mn, and C atoms.

energy of −0.64 eV (Table 3). This result is very similar to previous work on MgO (−0.68 eV) and Mn-doped MgO (−0.66 to −0.79 eV).[33,55] For V_O^x, the energetics of CO_2 adsorption in parallel or perpendicular configurations are similar (2.60 eV), with structural analysis showing that, in both cases, the CO_2 adopts a bent structure coordinated with both the defect and the surface atoms (Figure 5). In particular, one oxygen from the CO_2 fills the void while the second oxygen coordinates with a surface Mn, resulting in ∠(OCO) of 115.5°. This angular distortion prevents the adsorption energy from being as strong as for CO_2 z-aligned over MgO.[55]

As we remove an electron from V_O^x to form $V_O^{\bullet}$, the interaction between CO_2 and MnO weakens yet the adsorbate is still strongly coordinated with the surface, and the internal angle of ∠(OCO) is 119.7°. The maintenance of an adsorbed structure, yet weakening of the adsorption energy, shows how

DOI: 10.1021/acs.jpcc.8b07846
J. Phys. Chem. C 2019, 123, 8133−8144

Table 3. CO_2 Adsorption Energies on the MnO (100) surface, both Pristine and with Oxygen Vacancies, As Aligned along either the x- or z-Axis and Calculated with the B3LYP XC Functional[a]

		x-aligned	z-aligned
O_O^x	MnO	−0.64	–
	Mn−MgO[33]	−0.65	0.00
	MgO[55]	−0.68	0.11
V_O^x	MnO	−2.61	−2.61
	Mn−MgO[33]	−2.00	−3.13
	MgO[55]	−2.36	−3.52
	MgO[102]	−1.85	−3.23
$V_O^\bullet$	MnO	−1.60	–
	Mn−MgO[33]	−2.00	−1.12
	MgO[55]	−0.71	−1.11
	MgO[102]	−0.23	−1.04
$V_O^{\bullet\bullet}$	MnO	−0.02	−0.07
	Mn−MgO[33]	0.90	−0.09
	MgO[55]	0.11	0.04

[a]Also presented are previously calculated results for CO_2 adsorption on MgO and Mn_{surf}−MgO using the B3LYP XC functional and similar basis sets.[33,55] All values are given in eV.

important it is for electron transfer to occur from the support to the adsorbate. This factor is further exemplified for $V_O^{\bullet\bullet}$, where the CO_2 only interacts weakly with the support, at a separation distance of 3.5 Å. Thus, we can conclude that defect electrons positioned high in the band gap, as made available through the existence of oxygen vacancies, are important for catalytic CO_2 activation, in contrast with, e.g., MgO.[55] Furthermore, one can consider these observations are also indicative of preferential conditions for the reverse reaction of CO oxidation over MnO, where weaker CO_2 binding is preferential for the product to leave the support surface;[103] in this case, formation of $V_O^{\bullet\bullet}$ would be most beneficial.

5. SUMMARY AND CONCLUSIONS

We have used embedded cluster QM/MM calculations to investigate the electronic and energetic stability of MnO in pristine and defective bulk and in similar arrangements for (100) surfaces. We have modeled the system using low-energy principal diagonal antiferromagnetic ordering and the appropriate rhombohedrally distorted unit cell throughout.

For the bulk system, our calculations have shown that the valence band maximum and conduction band minimum are positioned at −4.79 eV and −0.87 eV relative to the vacuum level, with the valence band maximum formed of Mn 3d-states. We then use our model to calculate the preferential defect formation to be ionized vacancies, with a 2+ charge, when atomic defects are introduced with electron removal to the Fermi Level, ϵ_f, at the valence band maximum; at the conduction band minimum, double-charged Mn vacancies are far more stable than other defects, being exothermic to form in most cases. Schottky defects, whereby charged defects compensate each other to maintain charge neutrality at the macroscopic level, are most preferable for a combination of $V_O^{\bullet\bullet}$ and V_{Mn}'' defects: the formation energy is 2.40 eV when using the B3LYP XC functional. The defect levels for the charged vacancies were also investigated, with the V_O^x and $V_O^\bullet$ defects positioned mid band gap, similar to MgO; the V_{Mn}' and V_{Mn}'' defects are marginally lower in energy.

For the (100) surface, the structure proves similar to previous calculations, with interlayer contraction and slight oxygen protrusion from the surface. Again, we pursued calculations for the formation of oxygen vacancies, with results almost identical to the bulk, which highlights the relative stability of the surface; most defect levels were also similar to those in the bulk, with a notable exception being the $V_O^\bullet$ state, which was ∼0.6 eV lower for the surface. Finally, we presented testing of the chemical properties of the pristine and defective (100) surface for applications in CO_2 transformation. We show that the presence of defect-levels at surface vacancies on an MnO catalyst are crucial for activating the CO_2, with charge transfer resulting in strong adsorption and structural distortion. We are currently expanding this investigation to include MnO_x materials, where the higher oxidation state of the cation may influence the electronic and energetic properties.

■ ASSOCIATED CONTENT

Supporting Information

The Supporting Information is available free of charge on the ACS Publications website at DOI: 10.1021/acs.jpcc.8b07846.

Edited basis set for an Mn atom, as used in our calculations, documentation of periodic calculations for the formation enthalpies of MnO, figures illustrating defect formation enthalpies, and a pictorial representation of the defect levels for neutral and charged defects in MnO when using the B97-3 exchange-correlation functional (PDF)

■ AUTHOR INFORMATION

Corresponding Author

*(A.J.L.) E-mail: LogsdailA@cardiff.ac.uk.

ORCID

Andrew J. Logsdail: 0000-0002-2277-415X
Thomas W. Keal: 0000-0001-8747-3975
Alexey A. Sokol: 0000-0003-0178-1147

Notes

The authors declare no competing financial interest.
The raw data from which all energetic results were derived is available to access at DOI: 10.17035/d.2018.0052063074.

■ ACKNOWLEDGMENTS

The authors are grateful to David Scanlon and John Buckeridge for discussions associated with this work. A.J.L. acknowledges the Ramsay Memorial Trust and University College London for the provision of a Ramsay Fellowship. C.A.D. acknowledges the Molecular Modelling and Materials Science Industrial Doctorate Centre (M3S IDC) and the Science and Technology Facilities Council (STFC) for funding. A.J.L., T.W.K., P.S., A.A.S. and C.R.A.C. acknowledge funding from EPSRC Grants EP/IO30662/1 and EP/K038419/1. The authors acknowledge the use of computing facilities provided by ARCCA at Cardiff University, HPC Wales, and the ARCHER high-performance computing facilities via our membership of the UK HPC Materials Chemistry Consortium (EP/L000202). Finally, the authors wish to thank Joachim Sauer and Hajo Freund for many stimulating discussions on solid state and surface chemistry.

DOI: 10.1021/acs.jpcc.8b07846
J. Phys. Chem. C 2019, 123, 8133−8144

REFERENCES

(1) Al-Abadleh, H. A.; Grassian, V. H. Oxide Surfaces As Environmental Interfaces. *Surf. Sci. Rep.* **2003**, *52*, 63−161.
(2) Woodruff, D. P. Quantitative Structural Studies of Corundum and Rocksalt Oxide Surfaces. *Chem. Rev.* **2013**, *113*, 3863−3886.
(3) Noguera, C. *Physics and Chemistry at Oxide Surfaces*; Cambridge University Press: 1996.
(4) Pacchioni, G. Oxygen Vacancy: The Invisible Agent on Oxide Surfaces. *ChemPhysChem* **2003**, *4*, 1041−1047.
(5) Haider, M. H.; Dummer, N. F.; Knight, D. W.; Jenkins, R. L.; Howard, M.; Moulijn, J.; Taylor, S. H.; Hutchings, G. J. Efficient Green Methanol Synthesis from Glycerol. *Nat. Chem.* **2015**, *7*, 1028−1032.
(6) McFarland, E. W.; Metiu, H. Catalysis by Doped Oxides. *Chem. Rev.* **2013**, *113*, 4391−4427.
(7) Cui, Y.; Shao, X.; Baldofski, M.; Sauer, J.; Nilius, N.; Freund, H.-J. Adsorption, Activation, and Dissociation of Oxygen on Doped Oxides. *Angew. Chem., Int. Ed.* **2013**, *52*, 11385−11387.
(8) Stavale, F.; Shao, X.; Nilius, N.; Freund, H.-J.; Prada, S.; Giordano, L.; Pacchioni, G. Donor Characteristics of Transition-Metal-Doped Oxides: Cr-Doped MgO Versus Mo-Doped CaO. *J. Am. Chem. Soc.* **2012**, *134*, 11380−11383.
(9) Ganduglia-Pirovano, M. V.; Hofmann, A.; Sauer, J. Oxygen Vacancies in Transition Metal and Rare Earth Oxides: Current State of Understanding and Remaining Challenges. *Surf. Sci. Rep.* **2007**, *62*, 219−270.
(10) Wang, S.; Yan, S.; Ma, X.; Gong, J. Recent Advances in Capture of Carbon Dioxide Using Alkali-Metal-Based Oxides. *Energy Environ. Sci.* **2011**, *4*, 3805−3819.
(11) Choi, S.; Drese, J. H.; Jones, C. W. Adsorbent Materials for Carbon Dioxide Capture from Large Anthropogenic Point Sources. *ChemSusChem* **2009**, *2*, 796−854.
(12) Toroker, M. C.; Kanan, D. K.; Alidoust, N.; Isseroff, L. Y.; Liao, P.; Carter, E. A. First Principles Scheme to Evaluate Band Edge Positions in Potential Transition Metal Oxide Photocatalysts and Photoelectrodes. *Phys. Chem. Chem. Phys.* **2011**, *13*, 16644−16654.
(13) Stevanović, V.; Lany, S.; Ginley, D. S.; Tumas, W.; Zunger, A. Assessing Capability of Semiconductors to Split Water Using Ionization Potentials and Electron Affinities Only. *Phys. Chem. Chem. Phys.* **2014**, *16*, 3706−3714.
(14) Hammami, R.; Dhouib, A.; Fernandez, S.; Minot, C. CO2 Adsorption on (001) Surfaces of Metal Monoxides with Rock-Salt Structure. *Catal. Today* **2008**, *139*, 227−233.
(15) van den Berg, F.; Glezer, J.; Sachtler, W. the Role of Promoters in COH2 Reactions: Effects of MnO and MoO2 in Silica-Supported Rhodium Catalysts. *J. Catal.* **1985**, *93*, 340−352.
(16) De Jong, K.; Glezer, J.; Kuipers, H.; Knoester, A.; Emeis, C. Highly Dispersed Rh/SiO2 and Rh/MnO/SiO2 Catalysts: 1. Synthesis, Characterization, and CO Hydrogenation Activity. *J. Catal.* **1990**, *124*, 520−529.
(17) Xu, L.; Wang, Q.; Xu, Y.; Huang, J. A New Supported Fe-MnO Catalyst for the Production of Light Olefins from Syngas. I. Effect of Support on the Catalytic Performance. *Catal. Lett.* **1994**, *24*, 177−185.
(18) Seok, S.-H.; Han, S. H.; Lee, J. S. the Role of MnO in Ni/MnO-Al2O3 Catalysts for Carbon Dioxide Reforming of Methane. *Appl. Catal., A* **2001**, *215*, 31−38.
(19) Tanaka, Y.; Utaka, T.; Kikuchi, R.; Takeguchi, T.; Sasaki, K.; Eguchi, K. Water Gas Shift Reaction for the Reformed Fuels over Cu/MnO Catalysts Prepared Via Spinel-Type Oxide. *J. Catal.* **2003**, *215*, 271−278.
(20) Liu, Y.; Zhao, X.; Li, F.; Xia, D. Facile Synthesis of MnO/C Anode Materials for Lithium-Ion Batteries. *Electrochim. Acta* **2011**, *56*, 6448−6452.
(21) Lei, S.; Tang, K.; Fang, Z.; Liu, Q.; Zheng, H. Preparation of α-Mn2O3 and MnO from Thermal Decomposition of MnCO3 and Control of Morphology. *Mater. Lett.* **2006**, *60*, 53−56.
(22) Kanan, D. K.; Carter, E. A. Band Gap Engineering of MnO Via ZnO Alloying: A Potential New Visible-Light Photocatalyst. *J. Phys. Chem. C* **2012**, *116*, 9876−9887.
(23) Kanan, D. K.; Carter, E. A. Optical Excitations in MnO and MnO:ZnO Via Embedded CASPT2 Theory and Their Implications for Solar Energy Conversion. *J. Phys. Chem. C* **2013**, *117*, 13816−13826.
(24) Kanan, D. K.; Keith, J. A.; Carter, E. A. Water Adsorption on MnO:ZnO(001) from Single Molecules to Bilayer Coverage. *Surf. Sci.* **2013**, *617*, 218−224.
(25) Kanan, D. K.; Carter, E. A.; Dupuis, M.; Stoll, H.; Preuss, H.; Dam, H. J. J. V.; Wang, D.; Nieplocha, J.; Apra, E.; Windus, T. L.; et al. Ab Initio Study of Electron and Hole Transport in Pure and Doped MnO and MnO:ZnO Alloy. *J. Mater. Chem. A* **2013**, *1*, 9246−9256.
(26) Kanan, D. K.; Keith, J. A.; Carter, E. A. First-Principles Modeling of Electrochemical Water Oxidation on MnO:ZnO(001). *ChemElectroChem* **2014**, *1*, 407−415.
(27) Peng, H.; Ndione, P. F.; Ginley, D. S.; Zakutayev, A.; Lany, S. Design of Semiconducting Tetrahedral Mn 1 X Zn X O Alloys and Their Application to Solar Water Splitting. *Phys. Rev. X* **2015**, *5*, 021016.
(28) Honkala, K. Tailoring Oxide Properties: An Impact on Adsorption Characteristics of Molecules and Metals. *Surf. Sci. Rep.* **2014**, *69*, 366−388.
(29) Hattori, H. Solid Base Catalysts: Generation of Basic Sites and Application to Organic Synthesis. *Appl. Catal., A* **2001**, *222*, 247−259.
(30) Goniakowski, J.; Noguera, C. Atomic and Electronic Structure of Steps and Kinks on MgO(100) and MgO(110). *Surf. Sci.* **1995**, *340*, 191−204.
(31) Pacchioni, G.; Freund, H. Electron Transfer at Oxide Surfaces. the MgO Paradigm: From Defects to Ultrathin Films. *Chem. Rev.* **2013**, *113*, 4035−4072.
(32) Nilius, N.; Freund, H.-J. Activating Nonreducible Oxides Via Doping. *Acc. Chem. Res.* **2015**, *48*, 1532−1539.
(33) Logsdail, A. J.; Downing, C. A.; Keal, T. W.; Sherwood, P.; Sokol, A. A.; Catlow, C. R. A. Modelling the Chemistry of Mn-Doped MgO for Bulk and (100) Surfaces. *Phys. Chem. Chem. Phys.* **2016**, *18*, 28648−28660.
(34) Johnston, W. D.; Heikes, R. R. A Study of the LixMn(1-X)O System. *J. Am. Chem. Soc.* **1956**, *78*, 3255−3260.
(35) O'Keeffe, M.; Valigi, M. the Electrical Properties and Defect Structure of Pure and Chromium-Doped MnO. *J. Phys. Chem. Solids* **1970**, *31*, 947−962.
(36) Pearson, W. B. *A Handbook of Lattice Spacings and Structures of Metals and Alloys: International Series of Monographs on Metal Physics and Physical Metallurgy*, 4th ed.; Elsevier: 2013.
(37) Kittel, C. *Introduction to Solid State Physics*, 8th ed.; Wiley: New York, 2004.
(38) Harrison, W. A. Heisenberg Exchange in the Magnetic Monoxides. *Phys. Rev. B: Condens. Matter Mater. Phys.* **2007**, *76*, 054417.
(39) Corà, F.; Alfredsson, M.; Mallia, G.; Middlemiss, D. S.; Mackrodt, W. C.; Dovesi, R.; Orlando, R. The Performance of Hybrid Density Functionals in Solid State Chemistry. *Struct. Bonding* **2004**, *113*, 171−232.
(40) Feng, X. Electronic Structure of MnO and CoO from the B3LYP Hybrid Density Functional Method. *Phys. Rev. B: Condens. Matter Mater. Phys.* **2004**, *69*, 155107.
(41) Franchini, C.; Bayer, V.; Podloucky, R.; Paier, J.; Kresse, G. Density Functional Theory Study of MnO by a Hybrid Functional Approach. *Phys. Rev. B: Condens. Matter Mater. Phys.* **2005**, *72*, 045132.
(42) Franchini, C.; Podloucky, R.; Paier, J.; Marsman, M.; Kresse, G. Ground-State Properties of Multivalent Manganese Oxides: Density Functional and Hybrid Density Functional Calculations. *Phys. Rev. B: Condens. Matter Mater. Phys.* **2007**, *75*, 195128.
(43) Schrön, A.; Rödl, C.; Bechstedt, F. Energetic Stability and Magnetic Properties of MnO in the Rocksalt, Wurtzite, and Zinc-

DOI: 10.1021/acs.jpcc.8b07846
J. Phys. Chem. C 2019, 123, 8133−8144

Blende Structures: Influence of Exchange and Correlation. *Phys. Rev. B: Condens. Matter Mater. Phys.* **2010**, *82*, 165109.
(44) Logsdail, A. J.; Downing, C. A.; Catlow, C. R. A.; Sokol, A. A. Magnetic Coupling Constants for MnO As Calculated Using Hybrid Density Functional Theory. *Chem. Phys. Lett.* **2017**, *690*, 47−53.
(45) Morosin, B. Exchange Striction Effects in MnO and MnS. *Phys. Rev. B* **1970**, *1*, 236−243.
(46) Cheetham, A. K.; Hope, D. A. O. Magnetic Ordering and Exchange Effects in the Antiferromagnetic Solid Solutions MnXNi-(1X)O. *Phys. Rev. B: Condens. Matter Mater. Phys.* **1983**, *27*, 6964−6967.
(47) Shaked, H.; Faber, J.; Hitterman, R. L. Low-Temperature Magnetic Structure of Mno: A High-Resolution Neutron-Diffraction Study. *Phys. Rev. B: Condens. Matter Mater. Phys.* **1988**, *38*, 11901−11903.
(48) Sherwood, P.; De Vries, A. H.; Guest, M. F.; Schreckenbach, G.; Catlow, C. R. A.; French, S. A.; Sokol, A. A.; Bromley, S. T.; Thiel, W.; Turner, A. J.; et al. QUASI: A General Purpose Implementation of the QM/MM Approach and Its Application to Problems in Catalysis. *J. Mol. Struct.: THEOCHEM* **2003**, *632*, 1−28.
(49) Metz, S.; Kästner, J.; Sokol, A. A.; Keal, T. W.; Sherwood, P. ChemShell-a Modular Software Package for QM/MM Simulations. *Wiley Interdiscip. Rev.: Comput. Mol. Sci.* **2014**, *4*, 101−110.
(50) Valiev, M.; Bylaska, E. J.; Govind, N.; Kowalski, K.; Straatsma, T. P.; Van Dam, H. J. J. V.; Wang, D.; Nieplocha, J.; Apra, E.; Windus, T. L.; et al. NWChem: A Comprehensive and Scalable Open-Source Solution for Large Scale Molecular Simulations. *Comput. Phys. Commun.* **2010**, *181*, 1477−1489.
(51) Gale, J. D. GULP: A Computer Program for the Symmetry-Adapted Simulation of Solids. *J. Chem. Soc., Faraday Trans.* **1997**, *93*, 629−637.
(52) Gale, J. D.; Rohl, A. L. the General Utility Lattice Program (GULP). *Mol. Simul.* **2003**, *29*, 291−341.
(53) Gale, J. D. GULP: Capabilities and Prospects. *Z. Kristallogr. - Cryst. Mater.* **2005**, *220*, 552−554.
(54) Kästner, J.; Carr, J. M.; Keal, T. W.; Thiel, W.; Wander, A.; Sherwood, P. DL-FIND: An Open-Source Geometry Optimizer for Atomistic Simulations. *J. Phys. Chem. A* **2009**, *113*, 11856−11865.
(55) Downing, C. A.; Sokol, A. A.; Catlow, C. R. A. the Reactivity of CO2 on the MgO (100) Surface. *Phys. Chem. Chem. Phys.* **2014**, *16*, 184−195.
(56) Downing, C. A.; Sokol, A. A.; Catlow, C. R. A. the Reactivity of CO2 and H2 at Trapped Electron Sites at an Oxide Surface. *Phys. Chem. Chem. Phys.* **2014**, *16*, 21153−21156.
(57) Scanlon, D. O.; Dunnill, C. W.; Buckeridge, J.; Shevlin, S. A.; Logsdail, A. J.; Woodley, S. M.; Catlow, C. R. A.; Powell, M. J.; Palgrave, R. G.; Parkin, I. P.; et al. Band Alignment of Rutile and Anatase TiO2. *Nat. Mater.* **2013**, *12*, 798−801.
(58) Berger, D.; Logsdail, A. J.; Oberhofer, H.; Farrow, M. R.; Catlow, C. R. A.; Sherwood, P.; Sokol, A. A.; Blum, V.; Reuter, K. Embedded-Cluster Calculations in a Numeric Atomic Orbital Density-Functional Theory Framework. *J. Chem. Phys.* **2014**, *141*, 024105.
(59) Buckeridge, J.; Butler, K. T.; Catlow, C. R. A.; Logsdail, A. J.; Scanlon, D. O.; Shevlin, S. A.; Woodley, S. M.; Sokol, A. A.; Walsh, A. Polymorph Engineering of TiO_2: Demonstrating How Absolute Reference Potentials Are Determined by Local Coordination. *Chem. Mater.* **2015**, *27*, 3844−3851.
(60) Buckeridge, J.; Catlow, C. R. A.; Farrow, M. R.; Logsdail, A. J.; Scanlon, D. O.; Keal, T. W.; Sherwood, P.; Woodley, S. M.; Sokol, A. A.; Walsh, A. Deep Vs Shallow Nature of Oxygen Vacancies and Consequent N-Type Carrier Concentrations in Transparent Conducting Oxides. *Phys. Rev. Mater.* **2018**, *2*, 54604.
(61) Piccini, G.; Alessio, M.; Sauer, J. AbInitio Calculation of Rate Constants for Molecule-Surface Reactions with Chemical Accuracy. *Angew. Chem., Int. Ed.* **2016**, *55*, 5235−5237.
(62) Komsa, H.-P.; Pasquarello, A. Finite-Size Supercell Correction for Charged Defects at Surfaces and Interfaces. *Phys. Rev. Lett.* **2013**, *110*, 95505.
(63) Freysoldt, C.; Neugebauer, J. First-Principles Calculations for Charged Defects at Surfaces, Interfaces, and Two-Dimensional Materials in the Presence of Electric Fields. *Phys. Rev. B: Condens. Matter Mater. Phys.* **2018**, *97*, 205425.
(64) Lewis, G. V.; Catlow, C. R. A. Potential Models for Ionic Oxides. *J. Phys. C: Solid State Phys.* **1985**, *18*, 1149−1161.
(65) Becke, A. D. Density-Functional Thermochemistry. III. the Role of Exact Exchange. *J. Chem. Phys.* **1993**, *98*, 5648−5652.
(66) Lee, C.; Yang, W.; Parr, R. G. Development of the Colle-Salvetti Correlation-Energy Formula into a Functional of the Electron Density. *Phys. Rev. B: Condens. Matter Mater. Phys.* **1988**, *37*, 785−789.
(67) Stephens, P. J.; Devlin, F. J.; Chabalowski, C. F.; Frisch, M. J. Ab Initio Calculation of Vibrational Absorption and Circular Dichroism Spectra Using Density Functional Force Fields. *J. Phys. Chem.* **1994**, *98*, 11623−11627.
(68) Keal, T. W.; Tozer, D. J. Semiempirical Hybrid Functional with Improved Performance in an Extensive Chemical Assessment. *J. Chem. Phys.* **2005**, *123*, 121103.
(69) Weigend, F.; Ahlrichs, R. Balanced Basis Sets of Split Valence, Triple Zeta Valence and Quadruple Zeta Valence Quality for H to Rn: Design and Assessment of Accuracy. *Phys. Chem. Chem. Phys.* **2005**, *7*, 3297−3305.
(70) Dolg, M.; Wedig, U.; Stoll, H.; Preuss, H. Energy-Adjusted Ab Initio Pseudopotentials for the 1st-Row Transition-Elements. *J. Chem. Phys.* **1987**, *86*, 866−872.
(71) Fender, B. E. F.; Jacobson, A. J.; Wedgwood, F. A. Covalency Parameters in MnO, αMnS, and NiO. *J. Chem. Phys.* **1968**, *48*, 990−994.
(72) Jost, W. Diffusion and Electrolytic Conduction in Crystals (Ionic Semiconductors). *J. Chem. Phys.* **1933**, *1*, 466−475.
(73) Sokol, A. A.; Bromley, S. T.; French, S. A.; Catlow, C. R. A.; Sherwood, P. Hybrid QM/MM Embedding Approach for the Treatment of Localized Surface States in Ionic Materials. *Int. J. Quantum Chem.* **2004**, *99*, 695−712.
(74) Xu, Y.; Schoonen, M. A. the Absolute Energy Positions of Conduction and Valence Bands of Selected Semiconducting Minerals. *Am. Mineral.* **2000**, *85*, 543−556.
(75) Sugar, J.; Corliss, C. Atomic Energy Levels of the Iron-Period Elements, Potassium Through Nickel. *J. Phys. Chem. Ref. Data, Suppl.* **1985**, *14*, 664.
(76) van Elp, J.; Potze, R. H.; Eskes, H.; Berger, R.; Sawatzky, G. A. Electronic Structure of MnO. *Phys. Rev. B: Condens. Matter Mater. Phys.* **1991**, *44*, 1530−1537.
(77) Fromme, B.; Brunokowski, U.; Kisker, E. d D Excitations and Interband Transitions in MnO: A Spin-Polarized Electron-Energy-Loss Study. *Phys. Rev. B: Condens. Matter Mater. Phys.* **1998**, *58*, 9783−9792.
(78) Kurmaev, E. Z.; Wilks, R. G.; Moewes, A.; Finkelstein, L. D.; Shamin, S. N.; Kuneš, J. Oxygen X-Ray Emission and Absorption Spectra As a Probe of the Electronic Structure of Strongly Correlated Oxides. *Phys. Rev. B: Condens. Matter Mater. Phys.* **2008**, *77*, 165127.
(79) Massidda, S.; Continenza, A.; Posternak, M.; Baldereschi, A. Band-Structure Picture for MnO Reexplored: A Model GW Calculation. *Phys. Rev. Lett.* **1995**, *74*, 2323−2326.
(80) Faleev, S. V.; van Schilfgaarde, M.; Kotani, T. All-Electron Self-Consistent G W Approximation: Application to Si, MnO, and NiO. *Phys. Rev. Lett.* **2004**, *93*, 126406.
(81) Walsh, A.; Buckeridge, J.; Catlow, C. R. A.; Jackson, A. J.; Keal, T. W.; Miskufova, M.; Sherwood, P.; Shevlin, S. A.; Watkins, M. B.; Woodley, S. M.; et al. Limits to Doping of Wide Band Gap Semiconductors. *Chem. Mater.* **2013**, *25*, 2924−2926.
(82) Janthon, P.; Luo, S. A.; Kozlov, S. M.; Viñes, F.; Limtrakul, J.; Truhlar, D. G.; Illas, F. Bulk Properties of Transition Metals: A Challenge for the Design of Universal Density Functionals. *J. Chem. Theory Comput.* **2014**, *10*, 3832−3839.
(83) Lide, D. R. *CRC Handbook of Chemistry and Physics*, 84th ed.; CRC Press: Boca Raton, FL, 2003.

DOI: 10.1021/acs.jpcc.8b07846
J. Phys. Chem. C 2019, 123, 8133−8144

(84) Smyth, D. M. *the Defect Chemistry of Metal Oxides*; Oxford University Press: Oxford, U.K., 2000.
(85) Aschauer, U.; Vonrüti, N.; Spaldin, N. A. Effect of Epitaxial Strain on Cation and Anion Vacancy Formation in MnO. *Phys. Rev. B: Condens. Matter Mater. Phys.* **2015**, *92*, 054103.
(86) Stokłosa, A. Point Defects Diagrams for Pure and Doped Manganese Oxide Mn1δO in the Temperature Range of 1173−1830K. *Mater. Chem. Phys.* **2012**, *134*, 1136−1145.
(87) Ohama, N.; Hamaguchi, Y. Determination of the Exchange Integrals in β-MnO_2. *J. Phys. Soc. Jpn.* **1971**, *30*, 1311−1318.
(88) Hed, A. Z.; Tannhauser, D. S. High-Temperature Electrical Properties of Manganese Monoxide. *J. Chem. Phys.* **1967**, *47*, 2090−2103.
(89) Keller, M.; Dieckmann, R. Defect Structure and Transport Properties of Manganese Oxides: (I) the Nonstoichiometry of Manganosite (Mn1-ΔO). *Ber. Bunsenges. Phys. Chem.* **1985**, *89*, 883−893.
(90) Gvishi, M.; Tallan, N.; Tannhauser, D. the Hall Mobility of Electrons and Holes in MnO at High Temperature. *Solid State Commun.* **1968**, *6*, 135−137.
(91) De Wit, H.; Crevecoeur, C. n-Type Hall Effect in MnO. *Phys. Lett. A* **1967**, *25*, 393−394.
(92) Pai, M.; Honig, J. Electrical and Thermoelectric Properties of Undoped MnO Single Crystals. *J. Solid State Chem.* **1981**, *40*, 59−63.
(93) Martins, R. M. *Electronic Structure: Basic Theory and Practical Methods*; Cambridge University Press: 2004.
(94) Gibson, A.; Haydock, R.; LaFemina, J. P. Stability of Vacancy Defects in MgO: The Role of Charge Neutrality. *Phys. Rev. B: Condens. Matter Mater. Phys.* **1994**, *50*, 2582−2592.
(95) Sokol, A. A.; French, S. A.; Bromley, S. T.; Catlow, C. R. A.; van Dam, H. J. J.; Sherwood, P. Point Defects in ZnO. *Faraday Discuss.* **2007**, *134*, 267−282.
(96) Logsdail, A. J.; Mora-Fonz, D.; Scanlon, D. O.; Catlow, C. R. A.; Sokol, A. A. Structural, Energetic and Electronic Properties of (100) Surfaces for Alkaline Earth Metal Oxides As Calculated with Hybrid Density Functional Theory. *Surf. Sci.* **2015**, *642*, 58−65.
(97) Okazawa, T.; Kido, Y. Surface Structure and Lattice Vibrations of MnO(001) Analyzed by High-Resolution Medium Energy Ion Scattering Spectroscopy. *Surf. Sci.* **2004**, *556*, 101−108.
(98) Soares, E. A.; Paniago, R.; de Carvalho, V. E.; Lopes, E. L.; Abreu, G. J. P.; Pfannes, H.-D. Quantitative Low-Energy Electron Diffraction Analysis of MnO (100) Films Grown on Ag (100). *Phys. Rev. B: Condens. Matter Mater. Phys.* **2006**, *73*, 035419.
(99) Momida, H.; Oguchi, T. First-Principles Studies of Antiferromagnetic MnO and NiO Surfaces. *J. Phys. Soc. Jpn.* **2003**, *72*, 588−593.
(100) Bayer, V.; Franchini, C.; Podloucky, R. *Ab Initio* Study of the Structural, Electronic, and Magnetic Properties of MnO (100) and MnO (110). *Phys. Rev. B: Condens. Matter Mater. Phys.* **2007**, *75*, 035404.
(101) Fujimori, A.; Kimizuka, N.; Akahane, T.; Chiba, T.; Kimura, S.; Minami, F.; Siratori, K.; Taniguchi, M.; Ogawa, S.; Suga, S. Electronic Structure of MnO. *Phys. Rev. B: Condens. Matter Mater. Phys.* **1990**, *42*, 7580−7586.
(102) Florez, E.; Fuentealba, P.; Mondragon, F. Chemical Reactivity of Oxygen Vacancies on the MgO Surface: Reactions with CO2, NO2 and Metals. *Catal. Today* **2008**, *133-135*, 216−222.
(103) Ramesh, K.; Chen, L.; Chen, F.; Liu, Y.; Wang, Z.; Han, Y.-F. Re-Investigating the CO Oxidation Mechanism over Unsupported MnO, Mn2O3 and MnO2 Catalysts. *Catal. Today* **2008**, *131*, 477−482.

DOI: 10.1021/acs.jpcc.8b07846
J. Phys. Chem. C 2019, 123, 8133−8144